BNL-223010-2022-JAAM

A high-performance and durable direct NH3 tubular protonic ceramic fuel cell integrated with an internal catalyst layer

Y. Pan, K. Sasaki

To be published in "Applied Catalysis B-Environmental"

June 2022

Chemistry Department

Brookhaven National Laboratory

U.S. Department of Energy

USDOE Office of Science (SC), Basic Energy Sciences (BES) (SC-22)

Notice: This manuscript has been authored by employees of Brookhaven Science Associates, LLC under Contract No.DE-SC0012704 with the U.S. Department of Energy. The publisher by accepting the manuscript for publication acknowledges that the United States Government retains a non-exclusive, paid-up, irrevocable, world-wide license to publish or reproduce the published form of this manuscript, or allow others to do so, for United States Government purposes.

DISCLAIMER

This report was prepared as an account of work sponsored by an agency of the United States Government. Neither the United States Government nor any agency thereof, nor any of their employees, nor any of their contractors, subcontractors, or their employees, makes any warranty, express or implied, or assumes any legal liability or responsibility for the accuracy, completeness, or any third party's use or the results of such use of any information, apparatus, product, or process disclosed, or represents that its use would not infringe privately owned rights. Reference herein to any specific commercial product, process, or service by trade name, trademark, manufacturer, or otherwise, does not necessarily constitute or imply its endorsement, recommendation, or favoring by the United States Government or any agency thereof or its contractors or subcontractors. The views and opinions of authors expressed herein do not necessarily state or reflect those of the United States Government or any agency thereof.

A high-performance and durable direct NH_3 tubular protonic ceramic fuel cell integrated with an internal catalyst layer

Yuxin Pan[1], Hua Zhang[1], Kang Xu[1], Yucun Zhou[2], Bote Zhao[1,2], Wei Yuan[3], Kotaro Sasaki[4], YongMan Choi[5]*, Yu Chen[1]* and Meilin Liu[2]*

[1]School of Environment and Energy, South China University of Technology, Guangzhou 510006, China

[2]School of Materials Science and Engineering, Georgia Institute of Technology, 771 Ferst Dr NW, Atlanta, GA, 30332-0245, USA

[3]School of Mechanical and Automotive Engineering, South China University of Technology, Guangzhou 510640, China

[4]Chemistry Department, Brookhaven National Laboratory, Upton, NY 11973, USA

[5]College of Photonics, National Yang Ming Chiao Tung University, Tainan 71150, Taiwan

*Corresponding authors: YongMan Choi (ymchoi@nctu.edu.tw); Yu Chen (eschenyu@scut.edu.cn); Meilin Liu (meilin.liu@mse.gatech.edu)

Abstract

Nickel-based cermet anode-supported protonic ceramic fuel cells (PCFCs) show great potential for direct utilization of ammonia. However, the insufficient activity of anode and the deterioration of anode activity/durability caused by the undesired interaction between nickel and ammonia greatly limit the application. Here, we report tubular PCFCs embedded with a catalytic iron layer. Such cells show peak power densities of 1.507 Wcm^{-2} and 1.078 Wcm^{-2} at 700 ^oC when using H_2 and NH_3 as fuel, respectively, which are the highest tubular PCFC performance so far ever reported. In

addition, the stability of cells with the catalyst layer has been dramatically enhanced when compared with that of cells without the catalyst layer. The enhancement of activity and durability is attributed to the catalytic activity of iron for ammonia decomposition, through which the direct contact between nickel and ammonia has been minimized and the anode structure has therefore been protected.

Keywords: Protonic ceramic fuel cells; Tubular cells; Ammonia fuel; Catalytic layer

1. Introduction

Solid oxide fuel cells (SOFCs) can directly convert the chemical energy of fuels to electricity[1-4] and have been considered as one of the most promising energy devices in the future because of the relatively high energy conversion efficiency, low emissions, and huge fuel flexibility[5-8]. Among them, protonic ceramic fuel cells (PCFCs) are currently more attractive than oxygen ions-based SOFC due to the high conductivity of protons, enabling operations at intermediate temperatures. Although hydrogen is frequently used as fuel for PCFCs, the wide deployment of hydrogen energy is hindered by the large financial investment and safety risk in storage and transportation[9] due to the technological difficulties in liquefaction or compression of hydrogen[10]. Therefore, alternative fuels such as hydrocarbons or ammonia have been proposed for PCFCs.

Since the very first successful report of utilizing ammonia as fuel in a ceramic fuel cell system[11], the potential of ammonia has been gradually recognized by the SOFC community. As a carbon-free hydrogen carrier, ammonia has a high content of hydrogen and can be readily decomposed to H_2 and N_2 over traditional nickel-based cermet anodes at operating temperatures (500~800 ℃)[12]. In addition, ammonia can not only be liquefied in mild conditions[13] but also be widely used as

commercial chemical in the industry[14], making it a possible candidate as an alternative fuel for PCFCs. Numerous efforts have been devoted to the studies of ammonia-fueled PCFCs. For example, an early attempt by Xie et al.[15] demonstrated the feasibility of ammonia-fueled PCFCs, resulting in a peak power density of 315 mW cm^{-2} at 700 ℃. Aoki et al.[16] developed an ammonia-fueled PCFC based on the $BaZr_{0.1}Ce_{0.7}Y_{0.2}O_{3-\delta}$ electrolyte and Pd solid anode, which delivered a high output of 580 mW cm^{-2} at 600 ℃. Yang et al.[17] investigated the electrochemical and catalytic properties of a Ni-$BaCe_{0.75}Y_{0.25}O_{3-\delta}$ anode, exhibiting a higher ammonia decomposition catalytic activity over the Ni-YSZ (8 mol% Y_2O_3 stabilized ZrO_2) or Ni-$Ce_{0.9}Gd_{0.1}O_{1.95}$ anodes. Still, the efforts on developing ammonia PCFCs are very limited and the present achievements are yet to be satisfying. In particular, studies on the durability of ammonia PCFCs are insufficient. Therefore, more efforts are greatly necessary to develop high-performance and durable ammonia PCFCs.

Power generation using NH_3-fueled PCFC systems mainly consists of four steps: (i) adsorption of NH_3 on the anode surface; (ii) catalytic decomposition of NH_3 into H_2 and N_2; (iii) production of protons and electrons from the electrochemical reaction of H_2; (iv) protons transport through the dense electrolyte and electrons transport through an external circuit to the cathode[18]. As a key component for the anode, nickel shows a high electrical conductivity and an excellent catalytic activity towards the electrochemical reaction of H_2. Furthermore, nickel exhibits an efficient catalytic activity for ammonia decomposition, indicating that nickel-based anodes have great potential for ammonia-fueled ceramic fuel cells. However, cell durability in ammonia is a big concern[19], particularly due to the nitridation of nickel grains. Nitridation is dependent on experimental conditions (i.e., pressure and temperature), but it causes detrimental changes for the anode microstructure and consequently the degradation of cell performance[20]. A highly effective

strategy to mitigate the crucial issue and maintain a stable operation of fuel cells is to decompose NH_3 into H_2 before interacting with nickel anodes, minimizing the direct exposure of nickel to pure ammonia. The addition of another catalytic layer can facilitate the decomposition reaction of ammonia, a similarly practical approach for the development of direct hydrocarbons fueled SOFCs, where an internal catalyst layer is used to decompose hydrocarbons to H_2[21]. For practical preparation of the additional catalyst layer for efficient NH_3 decomposition, a tubular configuration has been proposed owing to its effective integration of additional catalysts with nickel backbone, suggesting that tubular cells may have inherent advantages to utilize ammonia fuel[22]. Besides, tubular cells also provide high mechanical strength, outstanding thermal-cycle stability, and easy assembling into stacks[23, 24], which make tubular cells promising for practical scaling up and commercialization. In particular, most of the reported NH_3-fueled tubular fuel cells are based on conventional oxygen-ion conducting SOFCs. On the contrary, tubular PCFCs operating in ammonia fuel are still undeveloped, and very few reports are available in the literature.

Herein, in the present study, tubular PCFCs based on a Ni-$BaZr_{0.1}Ce_{0.7}Y_{0.1}Yb_{0.1}$ (BZCYYb) anode support and a BZCYYb electrolyte have been successfully fabricated via cost-effective methods of phase inversion and dip-coating. In particular, outstanding cell performances have been achieved in both hydrogen and ammonia (1.507 Wcm^{-2} and 1.078 Wcm^{-2} at 700 ^oC, respectively). Furthermore, we demonstrated the durability in ammonia has been significantly improved by the simple addition of an internal catalytic iron layer. To complement the experimental findings, density functional theory (DFT) based simulations were carried out along with thermodynamic characteristics by calculating Gibbs free energies under experimental conditions. The theoretical analyses verify that the extraordinary stability by adding the catalytic iron layer may result from minimizing the direct

interaction of nickel and ammonia, avoiding its nitride formation. This systematic rational elucidation of the novel direct NH_3 tubular PCFC's superior performance with excellent stability over the conventional Ni-based configuration can be applied to other carbon-free fuels like hydrazine, widely extending PCFCs applications.

2. Experimental Section

2.1. Synthesis of materials

BZCYYb powders were synthesized through a solid-state reaction method[25]. The stoichiometric ratio of $BaCO_3$, ZrO_2, CeO_2, Y_2O_3, Yb_2O_3 (all purchased from Shanghai Macklin Biochemical Co. Ltd.) were mixed and ball-milled in ethanol for 24 h. After drying, the mixed powders were pressed into a pellet under 10 MPa and calcined at 1100 °C for 12 h. The above steps of ball-milling, pressing and calcination were repeated two times to obtain the final BZCYYb powders with pure phase. $PrBa_{0.5}Sr_{0.5}Co_{1.5}Fe_{0.5}O_{5+\delta}$ (PBSCF) cathode was synthesized by a solution combustion method. The stoichiometric ratio of $Pr(NO_3)_3 \cdot 6H_2O$, $Ba(NO_3)_2$, $Sr(NO_3)_2$, $Co(NO_3)_2 \cdot 6H_2O$, and $Fe(NO_3)_3 \cdot 6H_2O$ were selected as raw materials and dissolved in deionized water, along with the proper amount of glycine and citric acid (CA) as complexing agent. The molar ratio of glycine: CA: total metal ions was 0.75: 0.75: 1. Water in the solution was evaporated under constant stirring and heating at 80 °C, by which a transparent gel was obtained. The gel was then heated to 300 °C in an oven for complete combustion. The remaining ashes were further heated to 900 °C for 2h.

2.2. Fabrication of tubular cells

The preparation procedures of the tubular cell (Ni-BZCYYb / BZCYYb / PBSCF) were schematically shown in **Fig. 1**a A phase inversion technique was applied to fabricate the anode

substrate. In brief, an anode slurry was obtained by the ball-milling of NiO and BZCYYb powders in an organic solution for 24 h. More specifically, 27 g BZCYYb, 40.5 g NiO, 3 g polyethersulfone (PESf), 0.75 g polyvinyl pyrrolidone (PVP), and 18 g N-Methyl pyrrolidone (NMP) were mixed together. The slurry was then dip-coated on a glass rod (with a diameter of 4 mm), followed by the immediate immersion in water for 10 h. Phase inversion took place as mass exchanged between the slurry and water. As a result, the slurry eventually solidified and became a raw tube. After peeling off from the glass rod and drying overnight in ambient air, the raw tube was heated to 1000 ^{o}C to obtain the anode substrate. An anode functional layer (AFL) and an electrolyte layer were sequentially dip-coated on the anode substrate. Before the fabrication of AFL and electrolyte, wax was applied to seal one end of the tube, preventing the contact between the inner tube and the solution for dip-coating. Wax was then removed by heating in a drying oven at 70 ^{o}C. The tube with AFL and electrolyte layer was co-sintered at 1450 ^{o}C for 5 h. A cathode slurry, consisting of 55.6 wt% PBSCF, 42.2 wt% terpineols, and 2.2 wt% ethyl cellulose, was then brush-painted on the surface of the electrolyte. The cell was heated to 950 ^{o}C for 2 h to achieve a good adhesion between the electrolyte and the cathode. Finally, a catalytic layer was added by painting a slurry of iron trioxide (containing 44.4 wt% Fe_2O_3, 11.2 wt% graphite, 42.2 wt% terpineols, and 2.2 wt% ethyl cellulose) on the inner wall. The final tubular cell with an iron layer (denoted as Fe-cell) is represented in **Fig. 1**b, and the inner architecture and cross-sectional scanning electron microscope image of the tube were presented in **Fig. 1**c. In addition, tubular cells fabricated by the same methods except for the addition of a catalytic layer were also produced for comparison and denoted as a bare cell.

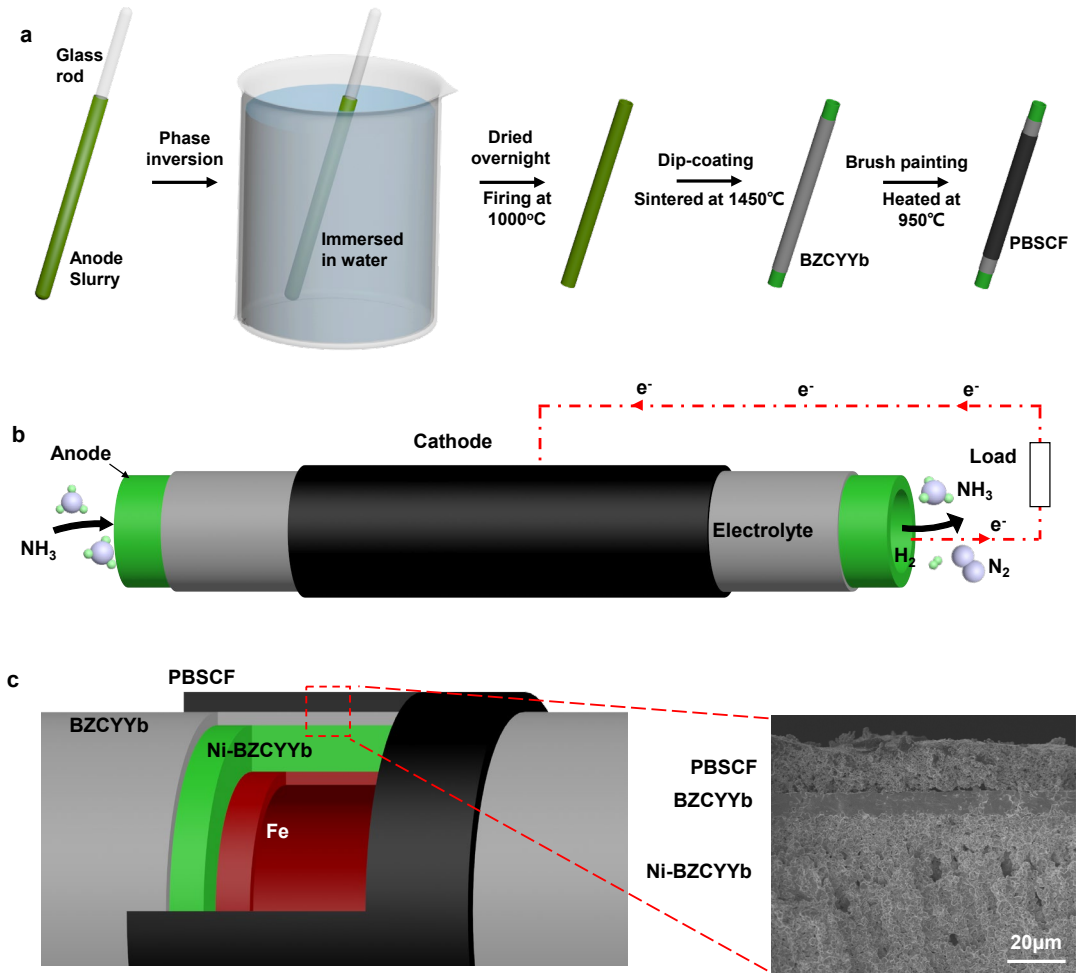

Fig. 1. (a) Schematics of the fabrication process of a tubular cell; (b) schematics of a tubular cell using direct ammonia as the fuel; (c) schematics of the inner architecture of the tube and a scanning electron micrograph of the actual cell consisting of a Ni-BZCYYb anode, a BZCYYb electrolyte, and a PBSCF cathode.

2.3. Characterization methods

Single-cell tests were carried out in a homemade testing setup. To collect the current, silver wires were attached to the inner wall of the tube and the surface of the cathode, respectively, using a silver paste (DAD-87). The silver wire was made into a coil shape, which can precisely fit into the inside of the tube. The catalyst slurry was then painted inside the tube after adding the silver wire.

Electrochemical performances were conducted by using an electrochemical work station (Princeton PARSTAT MC 200) after a reduction in hydrogen for 1 h at the anode side, using pure hydrogen or pure ammonia as fuels and ambient air as oxidant. Product gases were analyzed during cell testing, while the decomposition rate of ammonia was determined by the content of nitrogen using gas chromatography (Huifen GC-7820) and a gas flow meter. In the conversion rate testing, the flow rate of ammonia to the cells was controlled at 20 sccm, using a gas flowmeter. The length of the tubes was retained at 3.5 cm. The inner diameter was 3 mm. The thickness of the catalyst layer was around 25 μm. The surface area of the iron powder after electrochemical testing was determined as 1.58 m^2/g, from a Brunauer-Emmett-Teller (BET) measurement. Microstructures and morphologies of the tested cells were observed by a scanning electron microscope (SEM, Hitachi SU8010). Parts of the anodes from the cells after electrochemical testing were ground into powders and the phase structure of the samples was characterized by X-ray diffraction (XRD, Tongda TD-3500) using Cu-Kα as a radiation source.

2.4. Computational details

Spin-polarized density functional theory (DFT) calculations were carried out using the Vienna Ab initio Simulation Package (VASP)[26, 27] to examine the outstanding performance and stability of the direct NH_3-fueled protonic ceramic fuel cell using iron layer-added Ni/BZCYYb. We used Perdew-Burke-Ernzerh (PBE) functional[28] and the projector augmented plane wave (PAW) method.[29] The Monkhorst-Pack grid[30] with (3 × 3 × 3) and (3 × 3 × 1) was used for bulk and slab calculations, respectively, while a kinetic energy cutoff for 415 eV was applied. For the NH_3 decomposition processes, (2 × 2) four-layered surfaces of Ni (111) (16 Ni atoms), FeNi (111) (8 Fe

and 8 Ni atoms), and Fe(110) (16 Fe atoms) with a vacuum space of 15 Å were applied (*i.e.*, coverage of 1/4). The two bottom layers were fixed to the bulk parameters. The adsorption energy of atomic nitrogen on a surface was calculated by $E_{ads,N}$ = E(N-surface) – E(surface) – $E(N_2)/2$. While E(N-surface) and E(surface) are calculated electronic energies for adsorbed N on a surface and its blank surface, respectively, $E(N_2)$ is that for gas-phase nitrogen. The d-band centers of surfaces were calculated using the average energy of projected density of states (PDOSs) of the d-orbitals of bare metal surfaces.[31] The DMol^3 module[32] implemented in the Materials Studio package was used to calculate Gibbs's free energies using the optimized geometries from VASP. The double numerical polarization (DNP) 3.5 basis, the effective core potentials (ECP), and the PBE exchange-correlation functional were applied.

3. Result and discussion

3.1. Microstructure of the tubular cells

Shown in **Fig. 2** are SEM images of different parts of the tubular cell after electrochemical testing. As indicated by the overall cross-section of the cell in **Fig. 2**a, the thickness of the tube wall was around 500 μm. The thickness of the tube wall plays a pivotal role in the mechanical strength of the tube, which was greatly influenced by the viscosity of the original anode slurry in the phase inversion process. By adjusting the mass loading of the slurry of ceramic powders (NiO-BZCYYb), a robust tube was obtained.

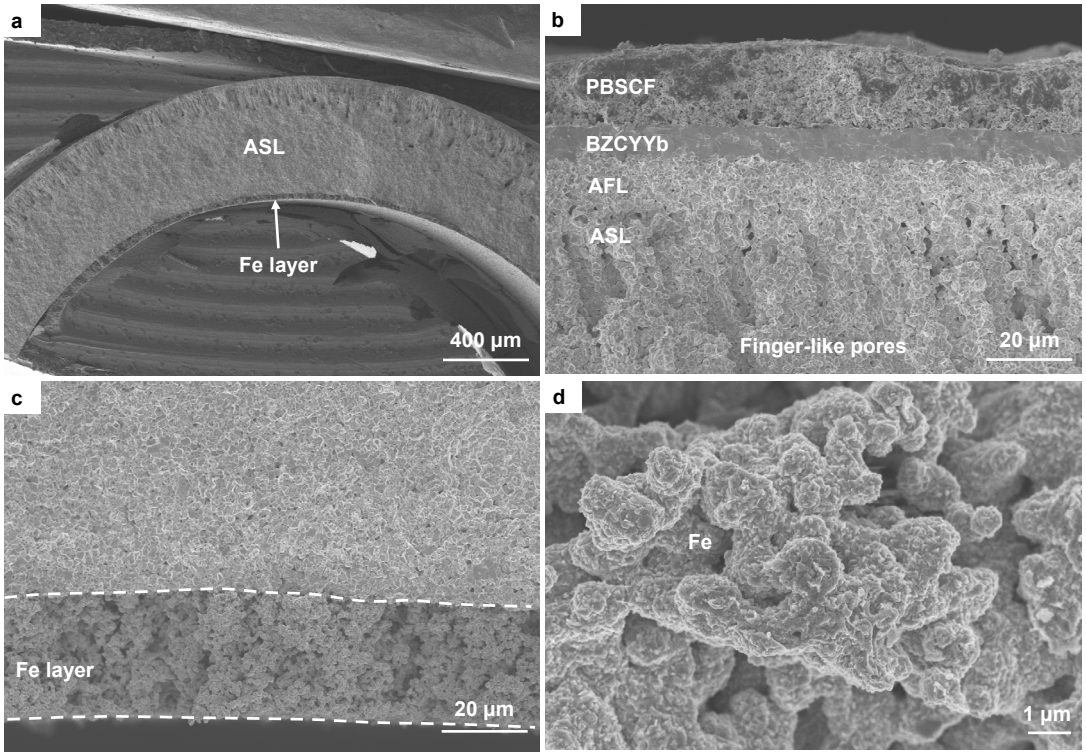

Fig. 2. Typical SEM images of the tubular cell: (a) an overall cross-section of the tube; (b) an enlarged view of the cell with ASL, AFL, BZCYYb, and PBSCF layer; (c) a detailed SEM image of the catalytic iron layer; (d) a close view of the iron surface after testing in ammonia.

Straight finger-like pores with a few dozen micrometers in length can be found between the anode supporting layer and electrolyte, as shown in **Fig. 2**a and **Fig. 2**b. It is a typical structure resulting from the phase inversion process[33], through which an asymmetric membrane containing a skin layer, a finger-like pores layer, and a porous sponge layer can be obtained. BZCYYb electrolyte and PBSCF cathode with a thickness of 8 μm and 20 μm can be observed respectively in the enlarged view near the electrolyte.

A catalytic iron layer with a few dozen of micrometers in thick was marked by the dotted lines in **Fig. 2**c**,** indicating that the internal catalytic layer was successfully added and well attached to the inner wall of the tube after electrochemical testing. Besides, macro voids were found within the iron

layer, which was induced by the removal of graphite and organic components in the original iron trioxide slurry. Such macro voids mitigated the negative effect of the additional layer and allowed the smooth diffusion of fuel gases to the anode bulk. The morphology of iron surfaces after testing in ammonia was presented in **Fig. 2**d. According to the literature, the catalytic decomposition of ammonia over iron can be regarded as two parallel reactions: ammonia catalytic decomposition and nitridation of iron[34]. Phase diagram of a Fe-N system[35] hinds that in the cell operation condition (600 ~ 700 °C) ε-Fe_2N could be the main form of iron nitrides. The formation of ε-Fe_2N was verified by characterizing the XRD patterns of the Fe-cell anodes after electrochemical testing in ammonia, as shown in **Figure S1**a, confirming the reaction between iron and ammonia. Meanwhile, the XRD patterns of the bare cell anodes after electrochemical testing in hydrogen and ammonia were also compared in **Figure S1**b but these two patterns delivered no obvious differences, implying that nickel nitride was not detected.

3.2. Electrochemical performances of the tubular cells

Single-cell tests fueled by pure hydrogen were conducted on tubular cells without and with the Fe layer, denoted as bare cell and Fe-cell. The related electrochemical performances of the bare cell and the Fe-cell were presented in **Fig. 3**. Peak power densities (PPDs) of 0.650, 1.060, 1.429 W cm^{-2} were achieved by the bare cell at 600, 650, 700 °C, respectively (**Fig. 3**a). These were very outstanding performances compared to other proton-conducting tubular SOFCs[36-41] (see **Table 1**). In the case of the Fe-cell, slightly increased PPDs of 0.776, 1.157, 1.507 W cm^{-2} were found at 600, 650, 700 °C, respectively (**Fig. 3**b). Since all conditions were kept the same for the bare cell and the Fe-cell, the performance enhancement can be attributed to the addition of the iron layer. To

further compare the electrochemical performances, electrochemical impedance spectra (EIS) of the two tubular cells were investigated under OCV conditions at various temperatures (see **Figure S2**). The polarization resistance (R_p) of the two cells can be roughly determined from EIS results, and the values were compared and presented in **Fig. 3**c. The Fe-cell showed small polarization resistances of 0.219, 0.073, 0.025 Ω cm^2 at the temperature of 600, 650, 700 ^oC, respectively, which were generally 35% smaller than the polarization resistances of the bare cell at various temperatures. Further electrochemical testings on the Fe-cells and the bare cells verified that the smaller polarization resistances in the Fe-cells were repeatable (**Figure S3**). The analysis of frequency behaviour suggests that anode reaction activity may be enhanced in the Fe-cells. In conclusion, the enhanced power densities of the Fe-cell can be attributed to the much smaller polarization resistances. In addition to power output, cell durability is also of great significance for SOFCs. The Fe-cell and the bare cell presented very similar stability behaviors in the durability testing when the cell was fueled by hydrogen under a constant current density of 0.5 A cm^{-2} at 650 ^oC. The Fe-cell delivered a slightly higher voltage during the testing period (see **Fig. 3**d), which further confirms that the catalytic iron layer has a little negative impact on the electrochemical performances of our tubular cells when fueled by pure hydrogen.

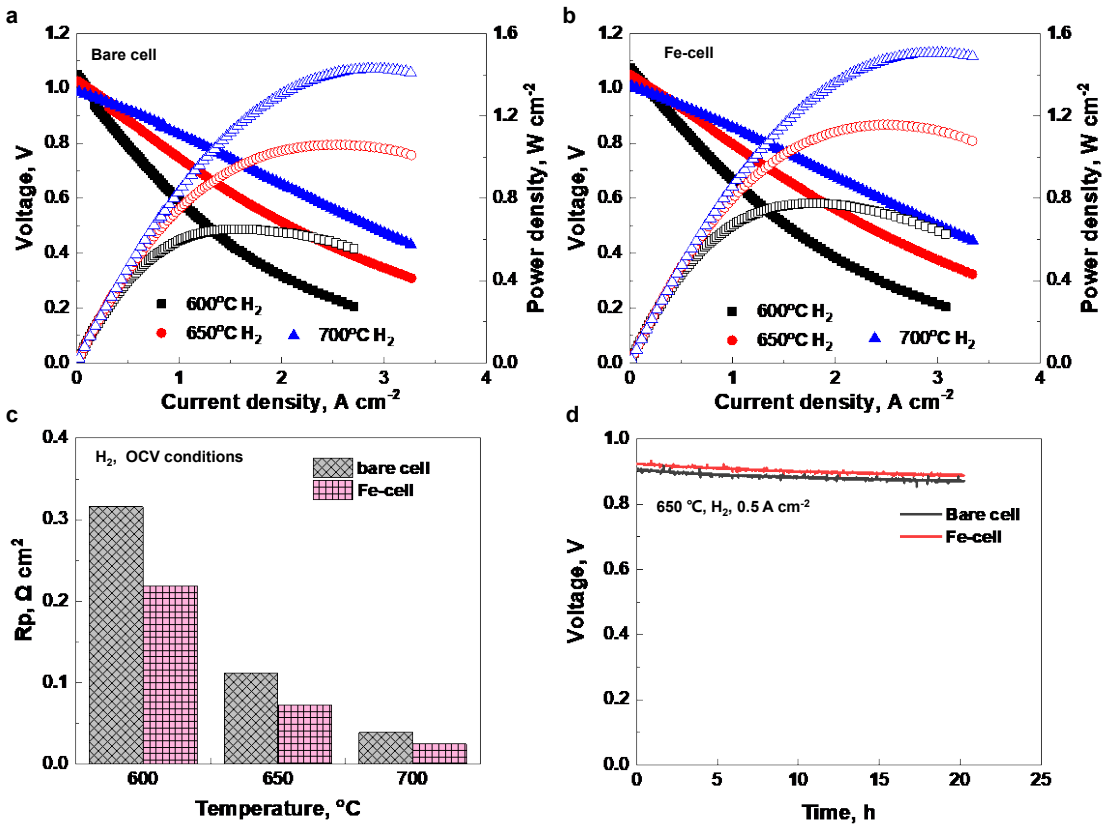

Fig. 3. Electrochemical performances of the tubular cells in pure hydrogen: typical I-V-P curves of (a) the bare cell and (b) the Fe-cell; (c) comparison of polarization resistances of the bare cell and the Fe-cell under OCV conditions; (d) a short term stability tests of 20h for the bare cell and the Fe-cell at 650 °C under a current density of 0.5 A cm^{-2}.

Electrochemical performances of both tubular cells in ammonia were characterized after the cells were tested in hydrogen and the results were presented in **Fig. 4**. When the fuel was switched from pure hydrogen to pure ammonia, there was a sudden drop in open-circuit voltage (OCV). It took a few minutes for the OCV values to recover, although the final values in ammonia were unable to return to the original values in hydrogen. Severe declines of OCV were found in the bare cell when fuel gas was switched from hydrogen to ammonia, more so at lower temperatures (dropped from 0.988 V to 0.947 V at 700 °C, from 1.028 V to 0.948 V at 650 °C, from 1.051 V to 0.918 V at 600 °C). The severe changes of OCV might be related to the insufficient ammonia decomposition catalytic

activity of the bare cell. It was confirmed by the ammonia conversion rates during cell testing, as shown in **Figure S4**. The ammonia conversion rates in the bare cell were only 61% and 76% at 600 and 650 ℃. As a result, insufficient hydrogen was produced at low temperatures, causing difficulty in maintaining high OCV values. Since ammonia decomposition is an endothermic reaction, the bare cell delivered a relatively high ammonia conversion rate at 700 ℃ (91.5%), coinciding with the smaller decline of OCV at 700 ℃. Even though the Fe-cell also underwent drops of OCV when fuel gas was switched to pure ammonia, the changes were less severe (dropped from 1.01 V to 0.99 V at 700 ℃, from 1.05 V to 1.011 V at 650 ℃, from 1.077 V to 1.011 V at 600 ℃). It can be attributed to the much higher ammonia conversion rates in the Fe-cell (**Figure S4**), indicating that the iron layer in the Fe-cell indeed improved the catalytic activity of cells toward NH_3 decomposition.

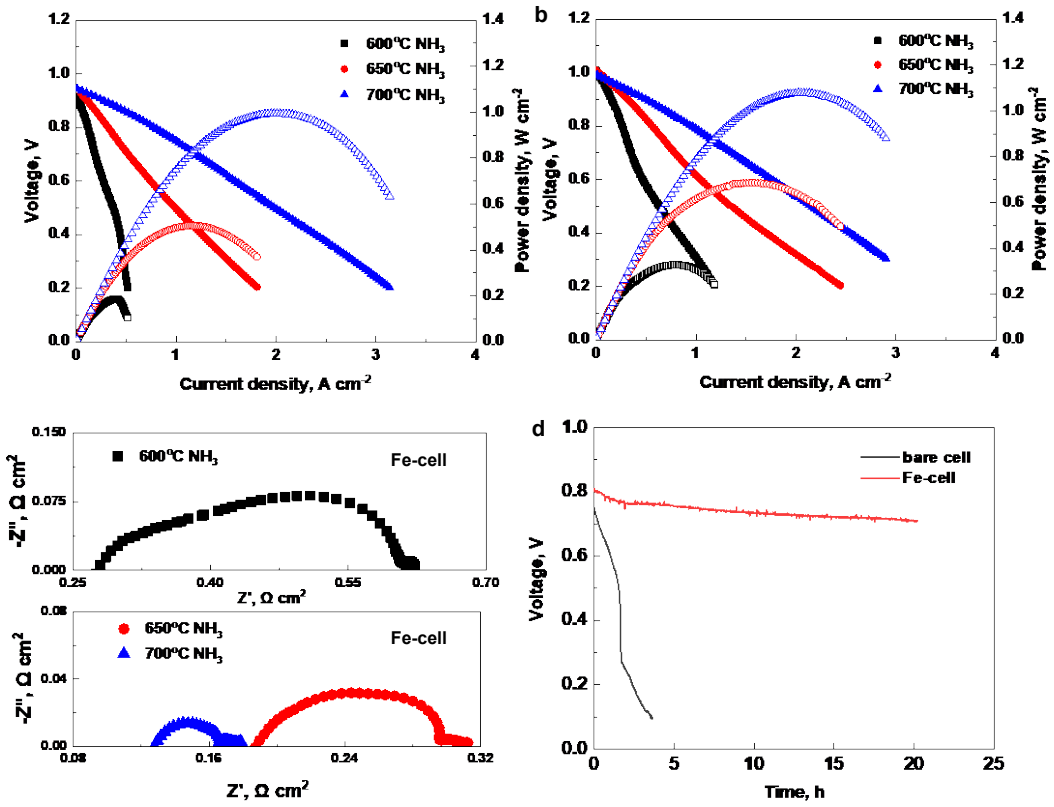

Fig. 4. Electrochemical performances of the tubular cells in pure ammonia: typical I-V-P curves of (a) the bare cell and (b) the Fe-cell; (c) electrochemical impedance spectra of the Fe-cell under OCV

conditions; (d) short-term stability tests of the bare cell and the Fe-cell at 650 ℃ under a constant current density of 0.5 A cm^{-2}.

Performance of the bare cell decreased significantly in ammonia, only delivering PPDs of 0.186, 0.506, 0.994 W cm^{-2} at 600, 650, 700 ℃ respectively (**Fig. 4**a). The decreased performance can be partly attributed to the diluted effect of nitrogen. Similarly, such performance decrease was also observed in the Fe-cells in ammonia, as shown by the lower power outputs and larger resistances (**Fig. 4**b and **Fig. 4**c). Still, the power outputs in ammonia were higher than those of the bare cells, achieving PPDs of 0.327, 0.685, 1.078 W cm^{-2} at 600, 650, 700 ℃ respectively. Notably, the performance enhancement of the Fe-cell over the bare cell was more pronounced at lower temperatures: the PPDs of the Fe-cell in ammonia were 75.8%, 35.4%, 8.5% higher than those of the bare cell at the temperatures of 600, 650, 700 ℃ respectively. The same tendency can be found in the OCV differences of the two cells in ammonia (the Fe-cell versus the bare cell: 1.011 V versus 0.918 V at 600 ℃, 1.011 V versus 0.948 V at 650 ℃, 0.99 V versus 0.947 V at 700 ℃). It can be concluded that when the tubular cells operated in ammonia, the catalytic iron layer played a more vital role in enhancing the performances at lower temperatures, as the endothermic ammonia decomposition reaction was more sensitive to the catalyst at lower temperatures. Listed **in Table 1** is the PPDs comparison of PCFCs when fueled by ammonia in recent studies[42-44], indicating that performances of our Fe-cell were very competitive.

Table 1 Electrochemical performances of some PCFCs fueled by hydrogen or ammonia in the literatures. (LSCF: $La_{0.6}Sr_{0.4}Co_{0.2}Fe_{0.8}O_{3-\delta}$, SDC: $Sm_{0.2}Ce_{0.8}O_{2-\delta}$, BZCY: $BaZr_{0.1}Ce_{0.7}Y_{0.2}O_{3-\delta}$, BZY: $BaZr_{0.8}Y_{0.2}O_{3-\delta}$,

PBC: $PrBaCo_2O_{5+\delta}$, BZCYYbPd: $Ba(Zr_{0.1}Ce_{0.7}Y_{0.1}Yb_{0.1})_{0.95}Pd_{0.05}O_{3-\delta}$, BCFZY: $BaCo_{0.4}Fe_{0.4}Zr_{0.1}Y_{0.1}O_{3-\delta}$, BCY: $BaCe_{0.8}Y_{0.2}O_{3-\delta}$, BSCF: $Ba_{0.5}Sr_{0.5}Co_{0.8}Fe_{0.2}O_{3-\delta}$)

Structure	**Electrolyte**	**Thickness (μm)**	**Cathode**	**Temperature (°C)**	**PPD (mW cm^{-2})**	**Ref**
Tubular	BZCYYb	12	LSCF-SDC	700	976 (H_2)	[36]
Tubular	BZCYYb	12	LSCF-BZCYYb	700	810 (H_2)	[37]
Tubular	BZCY	10	LSCF-BZCY	700	500 (H_2)	[38]
Tubular	**BZCYYb**	**8**	**PBSCF**	**700**	**1507** (H_2)	**This work**
Tubular	BZY	20	PBC-BZY	650	327 (H_2)	[39]
Tubular	BZCYYb	20	LSCF-BZCYYb	650	450 (H_2)	[40]
Tubular	BZCYYb	12	LSCF	650	721 (H_2)	[41]
Tubular	**BZCYYb**	**8**	**PBSCF**	**650**	**1157** (H_2)	**This work**
Planar	BZCYYbPd	17	BCFZY	650	724 (NH_3)	[42]
Planar	BCY	50	BSCF	650	190 (NH_3)	[43]
Planar	BZCY	35	BSCF	650	275 (NH_3)	[44]
Tubular	**BZCYYb**	**8**	**PBSCF**	**650**	**685 (NH_3)**	**This work**
				700	**1078 (NH_3)**	

Shown in **Fig. 4**d are the short-term stability tests of the bare cell and the Fe-cell under a constant current density of 0.5 A cm^{-2} at 650 °C when fueled by ammonia. A sharp degradation occurred to the bare cell as the voltage dropped from 0.749 V to 0.096 V within only 4 hours. The degradation was found to be largely attributed to the increase in ohmic resistance (**Figure S5**). The damage of ammonia on the cell can also be observed from the anode microstructure, as shown in **Figure S6**.

Anode microstructures of the bare cells and the Fe-cell, especially the morphologies of nickel surfaces, were compared after electrochemical testing. **Figure S6**a presented the anode microstructure of the bare cell after 20 h testing in hydrogen and the nickel particles were further examined in **Figure S6**b, where an ordinary morphology of nickel surface was observed. However, severe morphology changes occurred to the nickel surface after only 4 h operation in ammonia. As shown in **Figure S6**c and **Figure S6**d, lots of nano-sized pores were found on the nickel surface, which may be related to the interaction between ammonia and nickel particles. Nitridation of nickel particles happened in an ammonia atmosphere. Meanwhile, nickel nitrides can be easily decomposed due to their low stability in a reducing atmosphere or at high temperatures (over 400 ℃)[45]. In other words, nickel nitrides existed as a transient state and there was a repeat of nitride formation and decomposition, which might explain the inability to detect nickel nitride in the bare cell after electrochemical testing in ammonia in **Figure S1**. The continuous transition inevitably caused structural changes to the nickel particles and nano-sized pores were thereby formed on the surface.

On the other hand, the Fe-cell presented a very different stability behavior in ammonia. Although a rapid degradation was also found in the initial stage of testing, the Fe-cell maintained a relatively stable operation for almost 20 h, indicating that the catalytic iron layer significantly increased the stability of our tubular cells during the operation in ammonia fuel. The benefits of the iron layer were also demonstrated by the morphology of the nickel surface in **Figure S6**e and **Figure S6**f. The microstructure was very similar to the cell tested in hydrogen and almost no nano-sized pores were formed on the nickel surface. It demonstrates that the anode of the Fe-cell is well protected by the catalytic layer and therefore ammonia had little impact on the morphology of nickel.

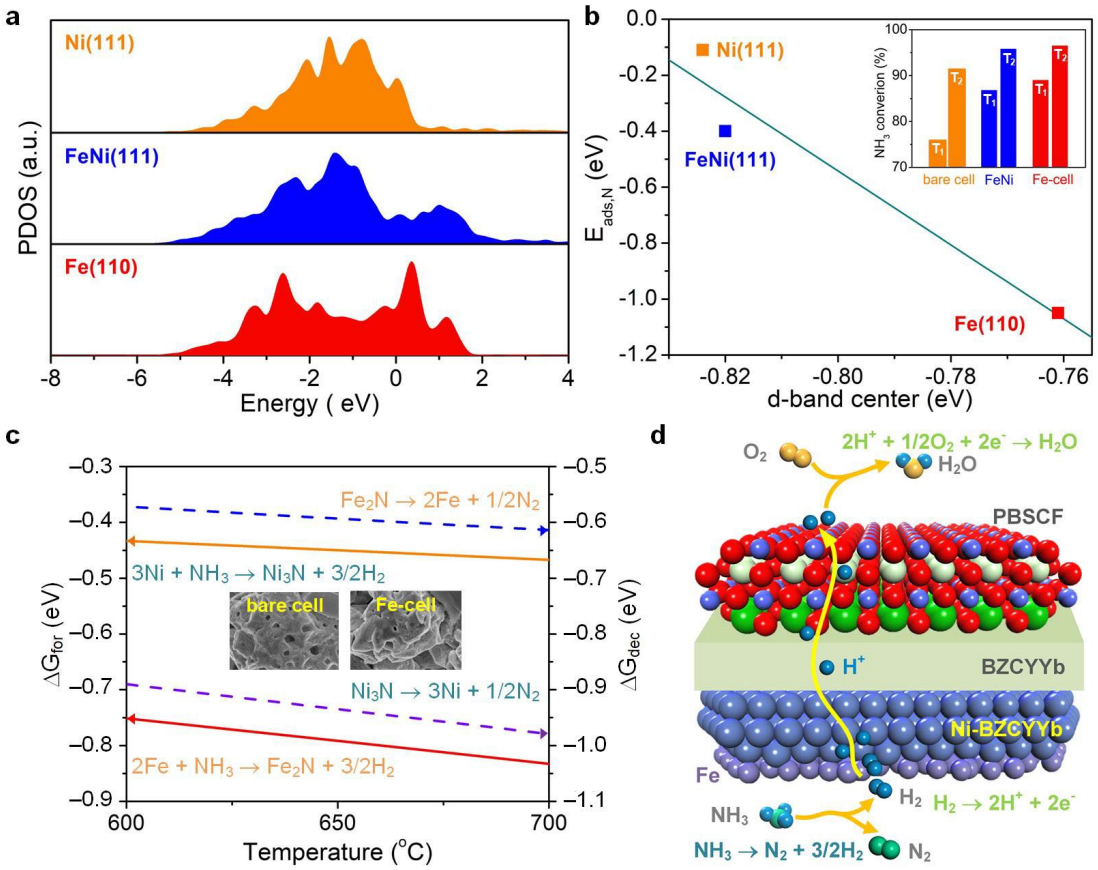

Fig. 5. (a) Projected density of states (PDOSs) of the d-orbitals of Ni(111), FeNi(111), and Fe(110). The Fermi energy level (E_F) is set to zero. (b) Adsorption energy of atomic nitrogen on Ni(111), FeNi(111), and Fe(110) against their d-band center. The inset of the figure is the experimental NH_3 conversion (%) for the bare cell, FeNi, and Fe-cell measured at 650°C (T_1) and 700°C (T_2). (c) Gibbs free energy changes of the formation (ΔG_{for}(eV)) and decomposition (ΔG_{dec}(eV)) of Ni_3N and Fe_2N from 600°C to 700°C. The SEM images are for the bare cell and the Fe-cell after NH_3-fueled experiments. (d) A schematic illustration of an ammonia-fueled PCFC using the iron layer.

3.3. DFT study of the Fe-cell durability in ammonia

Based on the experimental findings, we assumed that the effect of the iron layer can be schematically demonstrated in **Figure S7**. Briefly, in the bare cell, ammonia is directly fed to the Ni-BZCYYb

anode, followed by the catalytic decomposition to hydrogen over active nickel surfaces. As aforementioned, transient nickel nitrides would be formed and decomposed repeatedly via surface and bulk reactions, resulting in a dramatic morphology change (**Figure S6**d). These phenomena are difficult to observe using *ex-situ* characterization approaches. Thus, we investigated its electronic properties using DFT calculations. We assumed that the severe microstructural change of the bare cell after exposure to ammonia fuel is irreversible, suggesting that the surface nitridation ($xNi + NH_3 \leftrightarrow Ni_xN + 3/2H_2$ and $Ni_xN \leftrightarrow xNi + 1/2N_2$) becomes a bulk reaction (which is confirmed by the operation of the bare cells in ammonia for different period, as shown in **Figure S8**). Then, it could cause a detrimental impact on the anode structure and the degradation of cell performances. It was reported that its continuous volumetric changes of nickel particles[20] cause severe cracks. We approximatedamted the volumetric changes using DFT calculations as described below. The catalytic iron layer of the Fe-cell may also experience a similar nitridation for the formation of Fe_xN ($xFe + NH_3 \rightarrow Fe_xN + 3/2H_2$). In this configuration, we assume that the ammonia decomposition reaction mainly takes place on the additional iron layer. A small amount of NH_3 would reach the interfacial areas between the iron layer and Ni-BZCYYb anode (defined as FeNi region) due to the porous microstructure (**Fig. 2**c) along with hydrogen molecules decomposed from ammonia ($NH_3 \rightarrow 1/2N_2 + 3/2H_2$). Based on this observation, as summarized in **Fig. 5**, to theoretically elucidate the augmented stability of the Fe-cell compared to the bare cell by minimizing the direct interaction between nickel anodes and ammonia fuel, first-principles based thermodynamic calculations were performed below. It supports the iron layer effectively limits the formation of nickel nitrides, improving the cell stability. As shown in **Fig. 5** and **Figure S9**, three surface models of Ni(111), FeNi(111), and Fe(110) were constructed to examine the adsorption characteristics of atomic

nitrogen because it can be accurately applied as a descriptor for the rational design of catalytic materials for ammonia decomposition.[46, 47] Briefly, based on DFT calculations, the initial adsorption of NH_3 through nitrogen to a catalytic surface and the reaction barrier height for desorption of a nitrogen molecule (*i.e.*, association reaction of nitrogen species for producing gas-phase nitrogen) are strongly dependent on an amount of nickel and iron loadings. The more iron atoms on catalyst surfaces exhibit stronger adsorption of ammonia and the higher desorption barrier of nitrogen. Our detailed measurements of NH_3 conversion on the three different anode materials in **Figure S4** clarify that the Fe-cell exhibits the best activity towards NH_3 decomposition, while the FeNi alloy's conversion is close to that of the Fe-cell at 700 ^oC. This may denote the significance of initial NH_3's adsorption energy and desorption barrier heights of nitrogen molecules. **Fig. 5**a displays the calculated projected density of states (PDOSs) of the d-orbitals of three bare surfaces of Ni(111), FeNi(111), and Fe(110). We assume that FeNi(111) could be considered as interfacial moieties between Ni and Fe or the Ni-BZCYYb anode and the iron layer (**Fig. 2**c). We compared the adsorption energy of atomic nitrogen as a descriptor for understanding the efficient NH_3 decomposition and desorption of nitrogen products. Summarized in **Fig. 5**b is an excellent linear relationship of d-band centers and adsorption energies of atomic nitrogen and the experimental NH_3 conversion in our experimental temperature range. It indicates that the iron layer catalytically improves the NH_3 decomposition reaction. As Fe also has a good catalytic activity to hydrogen dissociation,[48] we experimentally compared the NH_3 conversion by mixing of nickel and iron oxides, followed by reduction (**Figure S3** and **Fig. 5**b). It indirectly explains that the interfacial FeNi regions are effectively utilized for decomposition of ammonia passing through the porous iron layer and hydrogen dissociation ($H_2 \rightarrow 2H$). Since these reactions take place on the catalyst surfaces,

we further investigated bulk nitride formation. Due to the unavailability of accurate thermodynamic properties of nitrides of nickel and iron, we carried out first-principles based Gibbs free energy calculations under the experimental temperature range of 600°C and 700°C (**Fig. 5**c) by assuming representative nickel and iron nitrides are Ni_3N and Fe_2N, respectively[35, 49]. Gibbs energy changes denote that Fe_2N can be more easily formed than Ni_3N via nitridation, while the decomposition of Ni_3N occurs more spontaneously than Fe_2N in reduction conditions ($Ni_3N + 3/2H_2 \rightarrow 3Ni + NH_3$) and via the thermal decomposition reaction ($Ni_3N \rightarrow 3Ni + 1/2N_2$). As mentioned above, we observed Fe_2N only after carrying out NH_3-fueled experiments (**Figure S1**). Therefore, as compared in **Fig. 5**c and **Figure S6**, one could conclude that the spontaneous reversible reactions of nickel versus nickel nitrides can cause irreversible alteration of microstructures of anode materials owing to the volume change of the unit cells of nickel and nickel nitrides (*i.e.*, 21.8% of Ni versus Ni_3N) (**Table S1**). In summary, the iron layer effectively minimizes the direct interaction of ammonia and nickel anodes, inhibiting nitride formation and resulting in outstanding stability. Furthermore, the synergistic contribution for hydrogen dissociation on Ni, FeNi interfaces, and Fe improves the overall performance compared to the bare cell. Its schematic illustration of the overall NH_3-fueled PCFC is displayed in **Fig. 5**d.

4. Conclusion

Tubular PCFCs based on the Ni-BZCYYb anode support have been successfully fabricated by adding an internal layer of iron to its inner side. The electrochemical performances of the tubular cells with and without the iron layer (denoted as Fe-cell and bare cell, respectively) have been compared to evaluate the effect of iron. When fueled by pure hydrogen, high PPDs of 0.776, 1.157,

and 1.507 W cm^{-2} were achieved by the Fe-cell at the temperatures of 600, 650, and 700 ℃, respectively, which were slightly higher than the PPDs of the bare cell. Long-term tests of both cells under a constant current density of 0.5 A cm^{-2} at 650 ℃ demonstrated that the Fe-cell and the bare cell showed a similar stability behavior in hydrogen. When fuel gas was switched to pure ammonia, PPDs of the Fe-cell were 0.327, 0.685, and 1.078 W cm^{-2} at the temperatures of 600, 650, and 700 ℃, respectively. Compared to the bare cell, the Fe-cell delivered much high power outputs, especially at lower temperatures. In particular, the stability of the cell on ammonia was greatly enhanced by the catalytic iron layer, while a sharp degradation occurred to the bare cell within only a few hours during long-term testing. The outstanding enhancement of the stability is attributed to the increased catalytic ammonia decomposition activity and the protective effect of the iron layer.

Declaration of Competing Interest

The authors declare no competing financial interest.

Acknowledgments

This work was supported by the National Natural Science Foundation of China (22005105, 22179039), the Pearl River Talent Recruitment Program (2019QN01C693, and 2021ZT09L392), and the Natural Science Foundation of Guangdong Province (2021A1515010395). Computational studies were supported by the Ministry of Science and Technology of Taiwan (MOST Grant No. 110-2221-E-A49-017-MY3), the National Center for High-performance Computing (NCHC), and the Higher Education Sprout Project of the National Yang Min Chiao Tung University and Ministry of Education (MOE), Taiwan. DFT calculations were performed using the resources of the Center

for Functional Nanomaterials, which is a U.S. DOE Office of Science Facility, at Brookhaven National Laboratory under Contract No. DE-SC0012704, Taiwan.

References

[1] E.P. Murray, T. Tsai, S.A. Barnett, A direct-methane fuel cell with a ceria-based anode, Nature, 400 (1999) 649-651.
[2] Z. Shao, S.M. Haile, A high-performance cathode for the next generation of solid-oxide fuel cells, Nature, 431 (2004) 170-173.
[3] Y. Zhang, B. Chen, D. Guan, M. Xu, R. Ran, M. Ni, W. Zhou, R. O'Hayre, Z. Shao, Thermal-expansion offset for high-performance fuel cell cathodes, Nature, 591 (2021) 246-251.
[4] Y. Chen, Y. Chen, D. Ding, Y. Ding, Y. Choi, L. Zhang, S. Yoo, D. Chen, B. deGlee, H. Xu, Q. Lu, B. Zhao, G. Vardar, J. Wang, H. Bluhm, E.J. Crumlin, C. Yang, J. Liu, B. Yildiz, M. Liu, A robust and active hybrid catalyst for facile oxygen reduction in solid oxide fuel cells, Energy & Environmental Science, 10 (2017) 964-971.
[5] C. Duan, R.J. Kee, H. Zhu, C. Karakaya, Y. Chen, S. Ricote, A. Jarry, E.J. Crumlin, D. Hook, R. Braun, N.P. Sullivan, R. O'Hayre, Highly durable, coking and sulfur tolerant, fuel-flexible protonic ceramic fuel cells, Nature, 557 (2018) 217-222.
[6] S. Sengodan, S. Choi, A. Jun, T.H. Shin, Y.-W. Ju, H.Y. Jeong, J. Shin, J.T.S. Irvine, G. Kim, Layered oxygen-deficient double perovskite as an efficient and stable anode for direct hydrocarbon solid oxide fuel cells, Nature Materials, 14 (2015) 205-209.
[7] Y. Chen, B. deGlee, Y. Tang, Z. Wang, B. Zhao, Y. Wei, L. Zhang, S. Yoo, K. Pei, J.H. Kim, Y. Ding, P. Hu, F.F. Tao, M. Liu, A robust fuel cell operated on nearly dry methane at 500 °C enabled by synergistic thermal catalysis and electrocatalysis, Nature Energy, 3 (2018) 1042-1050.
[8] Y. Chen, Y. Choi, S. Yoo, Y. Ding, R. Yan, K. Pei, C. Qu, L. Zhang, I. Chang, B. Zhao, Y. Zhang, H. Chen, Y. Chen, C. Yang, B. deGlee, R. Murphy, J. Liu, M. Liu, A Highly Efficient Multi-phase Catalyst Dramatically Enhances the Rate of Oxygen Reduction, Joule, 2 (2018) 938-949.
[9] A.M. Abdalla, S. Hossain, O.B. Nisfindy, A.T. Azad, M. Dawood, A.K. Azad, Hydrogen production, storage, transportation and key challenges with applications: A review, Energy Conversion and Management, 165 (2018) 602-627.
[10] G. Petitpas, Simulation of boil-off losses during transfer at a LH2 based hydrogen refueling station, International Journal of Hydrogen Energy, 43 (2018) 21451-21463.
[11] A. Wojcik, H. Middleton, I. Damopoulos, J. Van herle, Ammonia as a fuel in solid oxide fuel cells, Journal of Power Sources, 118 (2003) 342-348.
[12] J. Yang, T. Akagi, T. Okanishi, H. Muroyama, T. Matsui, K. Eguchi, Catalytic Influence of Oxide Component in Ni-Based Cermet Anodes for Ammonia-Fueled Solid Oxide Fuel Cells, Fuel Cells, 15 (2015) 390-397.
[13] A. Klerke, C.H. Christensen, J.K. Nørskov, T. Vegge, Ammonia for hydrogen storage: challenges and opportunities, Journal of Materials Chemistry, 18 (2008) 2304-2310.
[14] A. Valera-Medina, H. Xiao, M. Owen-Jones, W.I.F. David, P.J. Bowen, Ammonia for power, Progress in Energy and Combustion Science, 69 (2018) 63-102.

[15] K. Xie, Q. Ma, B. Lin, Y. Jiang, J. Gao, X. Liu, G. Meng, An ammonia fuelled SOFC with a BaCe0.9Nd0.1O3−δ thin electrolyte prepared with a suspension spray, Journal of Power Sources, 170 (2007) 38-41.
[16] Y. Aoki, T. Yamaguchi, S. Kobayashi, D. Kowalski, C. Zhu, H. Habazaki, High-Efficiency Direct Ammonia Fuel Cells Based on BaZr0.1Ce0.7Y0.2O3−δ/Pd Oxide-Metal Junctions, Global Challenges, 2 (2018) 1700088.
[17] J. Yang, A.F.S. Molouk, T. Okanishi, H. Muroyama, T. Matsui, K. Eguchi, Electrochemical and Catalytic Properties of Ni/BaCe0.75Y0.25O3−δ Anode for Direct Ammonia-Fueled Solid Oxide Fuel Cells, ACS Applied Materials & Interfaces, 7 (2015) 7406-7412.
[18] M. Ni, D.Y.C. Leung, M.K.H. Leung, Thermodynamic analysis of ammonia fed solid oxide fuel cells: Comparison between proton-conducting electrolyte and oxygen ion-conducting electrolyte, Journal of Power Sources, 183 (2008) 682-686.
[19] Z. Wan, Y. Tao, J. Shao, Y. Zhang, H. You, Ammonia as an effective hydrogen carrier and a clean fuel for solid oxide fuel cells, Energy Conversion and Management, 228 (2021) 113729.
[20] J. Yang, A.F.S. Molouk, T. Okanishi, H. Muroyama, T. Matsui, K. Eguchi, A Stability Study of Ni/Yttria-Stabilized Zirconia Anode for Direct Ammonia Solid Oxide Fuel Cells, ACS Applied Materials & Interfaces, 7 (2015) 28701-28707.
[21] W. Wang, C. Su, Y. Wu, R. Ran, Z. Shao, Progress in solid oxide fuel cells with nickel-based anodes operating on methane and related fuels, Chemical reviews, 113 (2013) 8104-8151.
[22] T. Suzuki, T. Yamaguchi, K. Hamamoto, Y. Fujishiro, M. Awano, N. Sammes, A functional layer for direct use of hydrocarbon fuel in low temperature solid-oxide fuel cells, Energy & Environmental Science, 4 (2011) 940-943.
[23] K. Kendall, Progress in Microtubular Solid Oxide Fuel Cells, International Journal of Applied Ceramic Technology, 7 (2010) 1-9.
[24] N.M. Sammes, Y. Du, Fabrication and Characterization of Tubular Solid Oxide Fuel Cells, International Journal of Applied Ceramic Technology, 4 (2007) 89-102.
[25] L. Yang, S. Wang, K. Blinn, M. Liu, Z. Liu, Z. Cheng, M. Liu, Enhanced Sulfur and Coking Tolerance of a Mixed Ion Conductor for SOFCs: BaZr_{0.1}Ce_{0.7}Y_{0.2–}_xYb_xO<sub>3–δ</sub&gt, Science, 326 (2009) 126.
[26] G. Kresse, J. Hafner, Ab initio molecular dynamics for liquid metals, Phys. Rev. B, 47 (1993) 558-561.
[27] G. Kresse, J. Furthmuller, Efficient iterative schemes for ab initio total-energy calculations using a plane-wave basis set, Phys. Rev. B, 54 (1996) 11169-11186.
[28] J.P. Perdew, K. Burke, M. Ernzerhof, Generalized Gradient Approximation Made Simple, Phys. Rev. Lett., 77 (1996) 3865-3868.
[29] P.E. Blöchl, Projector augmented-wave method, Phys. Rev. B, 50 (1994) 17953-17979.
[30] H.J. Monkhorst, J.D. Pack, Special points for Brillouin-zone integrations, Phys. Rev. B, 13 (1976) 5188-5192.
[31] A. Nilsson, L.G.M. Pettersson, B. Hammer, T. Bligaard, C.H. Christensen, J.K. Nørskov, The electronic structure effect in heterogeneous catalysis, Catal. Lett., 100 (2005) 111-114.
[32] B. Delley, An all-electron numerical method for solving the local density functional for polyatomic molecules, J. Chem. Phys., 92 (1990) 508-517.

[33] H. Strathmann, K. Kock, The formation mechanism of phase inversion membranes, Desalination, 21 (1977) 241-255.
[34] W. Arabczyk, R. Pelka, Studies of the kinetics of two parallel reactions: ammonia decomposition and nitriding of iron catalyst, The journal of physical chemistry. A, 113 2 (2009) 411-416.
[35] B.J. Kooi, M.A.J. Somers, E.J. Mittemeijer, An evaluation of the Fe-N phase diagram considering long-range order of N atoms in γ′-Fe4N1-x and ε-Fe2N1-z, Metallurgical and Materials Transactions A, 27 (1996) 1063-1071.
[36] C. Chen, Y. Dong, L. Li, Z. Wang, M. Liu, B.H. Rainwater, Y. Bai, Electrochemical properties of micro-tubular intermediate temperature solid oxide fuel cell with novel asymmetric structure based on BaZr0.1Ce0.7Y0.1Yb0.1O3−δ proton conducting electrolyte, International Journal of Hydrogen Energy, 44 (2019) 16887-16897.
[37] C. Chen, M. Liu, Y. Bai, L. Yang, E. Xie, M. Liu, Anode-supported tubular SOFCs based on BaZr0.1Ce0.7Y0.1Yb0.1O3−δ electrolyte fabricated by dip coating, Electrochemistry Communications, 13 (2011) 615-618.
[38] S.H. Min, R.-H. Song, J.G. Lee, M.-G. Park, K.H. Ryu, Y.-K. Jeon, Y.-g. Shul, Fabrication of anode-supported tubular Ba(Zr0.1Ce0.7Y0.2)O3−δ cell for intermediate temperature solid oxide fuel cells, Ceramics International, 40 (2014) 1513-1518.
[39] L. Bi, E.H. Da'as, S.P. Shafi, Proton-conducting solid oxide fuel cell (SOFC) with Y-doped BaZrO3 electrolyte, Electrochemistry Communications, 80 (2017) 20-23.
[40] C. Ren, S. Wang, T. Liu, Y. Lin, F. Chen, Fabrication of micro-tubular solid oxide fuel cells using sulfur-free polymer binder via a phase inversion method, Journal of Power Sources, 290 (2015) 1-7.
[41] Y. Dong, C. Chen, M. Liu, B.H. Rainwater, Y. Bai, Enhancement of Electrochemical Properties, Impedance and Resistances of Micro-tubular IT-SOFCs with Novel Asymmetric Structure Based on BaZr0.1Ce0.7Y0.1Yb0.1O3−δ Proton Conducting Electrolyte, Fuel Cells, 20 (2020) 70-79.
[42] F. He, Q. Gao, Z. Liu, M. Yang, R. Ran, G. Yang, W. Wang, W. Zhou, Z. Shao, A New Pd Doped Proton Conducting Perovskite Oxide with Multiple Functionalities for Efficient and Stable Power Generation from Ammonia at Reduced Temperatures, Advanced Energy Materials, 11 (2021) 2003916.
[43] Y. Yoo, M. Tuck, N. Lim, A. McFarlan, N. Maffei, Fabrication of Anode Supported Direct Ammonia Solid Oxide Fuel Cells Based on Proton Conducting Y-doped BaCeO3 Electrolyte, ECS Transactions, 7 (2019) 2305-2312.
[44] Y. Lin, R. Ran, Y. Guo, W. Zhou, R. Cai, J. Wang, Z. Shao, Proton-conducting fuel cells operating on hydrogen, ammonia and hydrazine at intermediate temperatures, International Journal of Hydrogen Energy, 35 (2010) 2637-2642.
[45] A. Baiker, M. Maciejewski, Formation and thermal stability of copper and nickel nitrides, Journal of the Chemical Society, Faraday Transactions 1: Physical Chemistry in Condensed Phases, 80 (1984) 2331-2341.
[46] X. Duan, G. Qian, C. Fan, Y. Zhu, X. Zhou, D. Chen, W. Yuan, First-principles calculations of ammonia decomposition on Ni(110) surface, Surf. Sci., 606 (2012) 549-553.
[47] X. Duan, J. Ji, G. Qian, C. Fan, Y. Zhu, X. Zhou, D. Chen, W. Yuan, Ammonia decomposition on Fe(110), Co(111) and Ni(111) surfaces: A density functional theory study, J. Mol. Catal. A-Chem, 357 (2012) 81-86.
[48] Z. Cheng, J.-H. Wang, Y. Choi, L. Yang, M.C. Lin, M. Liu, From Ni-YSZ to sulfur-tolerant anode materials for SOFCs: electrochemical behavior, in situ characterization, modeling, and future perspectives, Energy & Environmental Science, 4 (2011) 4380-4409.

[49] A. Fernández Guillermet, K. Frisk, Thermodynamic properties of ni nitrides and phase stability in the Ni-N system, International Journal of Thermophysics, 12 (1991) 417-431.